Ultrasound in Med. & Biol., Vol. 32, No. 3, pp. 397–408, 2006

0301-5629/06/$–see front matter

ELSEVIER

doi:10.1016/j.ultrasmedbio.2005.11.011

● *Original Contribution*

SEGMENTATION OF ELASTOGRAPHIC IMAGES USING A COARSE-TO-FINE ACTIVE CONTOUR MODEL

Wu Liu,* James A. Zagzebski,*† Tomy Varghese,*‡ Charles R. Dyer,§
Udomchai Techavipoo,*‖ and Timothy J. Hall*

*Departments of Medical Physics,†Radiology, ‡Biomedical Engineering, §Computer Sciences and ‖Electrical and Computer Engineering, University of Wisconsin-Madison, Madison, WI, USA

(*Received* 2 *August* 2005, *revised* 7 *November* 2005, *in final form* 17 *November* 2005)

Abstract—Delineation of radiofrequency-ablation-induced coagulation (thermal lesion) boundaries is an important clinical problem that is not well addressed by conventional imaging modalities. Elastography, which produces images of the local strain after small, externally applied compressions, can be used for visualization of thermal coagulations. This paper presents an automated segmentation approach for thermal coagulations on 3-D elastographic data to obtain both area and volume information rapidly. The approach consists of a coarse-to-fine method for active contour initialization and a gradient vector flow, active contour model for deformable contour optimization with the help of prior knowledge of the geometry of general thermal coagulations. The performance of the algorithm has been shown to be comparable to manual delineation of coagulations on elastograms by medical physicists (r = 0.99 for volumes of 36 radiofrequency-induced coagulations). Furthermore, the automatic algorithm applied to elastograms yielded results that agreed with manual delineation of coagulations on pathology images (r = 0.96 for the same 36 lesions). This algorithm has also been successfully applied on *in vivo* elastograms. (E-mail: wuliu@wisc.edu)

Key Words: **Ablation, Active contour models, Breast tumor, Elasticity imaging, Elastography, Gradient vector flow, Image segmentation, Multiresolution, Snakes, Strain, 3-D ultrasound.**

INTRODUCTION

Image-guided radiofrequency (RF) tumor ablation has provided an effective and safe means to treat a large variety of benign and malignant conditions and holds promise as a treatment on an outpatient basis (De Sanctis et al. 1998; Goldberg et al. 2000, 2003). RF ablation is an interstitial focal ablative therapy in which an electrode is placed into a tumor to cause heating and cauterization of the tumor from ionic agitation. The rapid vibration of ions creates friction, thereby heating the region-of-interest (ROI). The goal of tumor ablation is complete destruction of tumor targets without excessive damage to surrounding healthy tissue.

Imaging modalities that dynamically and precisely monitor the cellular damage during and after treatment are important to the success of RF ablation therapy (Goldberg et al. 2000, 2003). Ultrasound (US) is a commonly used modality for guiding RF ablation procedures for hepatic tumors (Goldberg et al. 2000; Giorgio et al. 2003; Hansler et al. 2004). For lesions that are suboptimally visualized by US, ablation procedures may be performed under computed tomography (CT) guidance (Cha et al. 2000; Antoch et al. 2002) to optimize RF electrode positioning and monitor the extent of coagulation. However, CT generally is not used for real-time monitoring.

Elastography, a new imaging modality that is based on US, is sensitive to small changes in elastic modulus (Kallel et al. 1998) and thus, it has the potential to image and differentiate thermal coagulation necrosis from healthy surrounding tissues. Figure 1 shows US B-mode, elastographic and pathologic views of a typical thermal coagulation. On the conventional B-mode image, the RF-induced coagulation exhibits both hyperechoic and hypoechoic regions at the apparent coagulation site. However, it has poor contrast and it is extremely difficult for the interventionist to judge the adequacy of the RF treatment, because margin delineation is uncertain. In contrast, the thermal lesion can be clearly seen as a low strain (dark) region on the elastogram, as seen in Fig. 1.

Address correspondence to: Dr. Wu Liu, Department of Medical Physics, University of Wisconsin-Madison, 1300 University Ave., Madison, WI 53706-1532 USA. E-mail: wuliu@wisc.edu

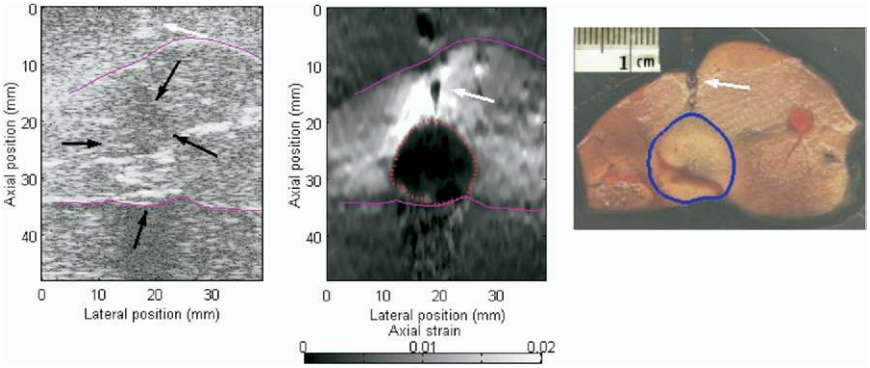

Fig. 1. (left) US B-mode, (center) elastographic, and (right) pathologic images of a typical thermal coagulation on a freshly excised canine liver. Solid curves are the boundary of the liver as defined from B-mode image. Note that the coagulated region exhibits both hyperechoic and hypoechoic areas in B-mode, and its boundary is difficult to delineate. The coagulated region can be clearly seen as a low strain (dark) region on the elastogram. Dotted-line contour is manually depicted coagulation boundary. Coagulated region on the fresh pathology photograph shows as a white area of coagulation necrosis and a darker zone of charring. Solid-line contour is the outer boundary of the white region.

RF ablation is known to increase the stiffness of tissue at the treated site and US elastography (Ophir et al. 1991; Varghese et al. 2001) detects and images these changes. We have shown that 2-D and 3-D elastography exhibit high coagulation-to-liver contrast for RF-induced thermal lesions, as well as good correlation with pathology (Varghese et al. 2002; Liu et al. 2004; Varghese and Shi 2004).

The use of 3-D US is rapidly increasing, both in the research environment and in clinical settings (Fenster et al. 2001). 3-D usage also applies to elastography because of advantages of volumetric data over conventional 2-D data for quantitatively monitoring therapeutic procedures and for follow-up studies. However, the immense quantity of 3-D data can lead to new problems, particularly if extracting surfaces and volumes from the 3-D data set is required. For example, manually tracing RF-induced coagulation boundaries, which requires substantial expertise and experience in image interpretation, is time-consuming and tedious. Therefore, accurate, reproducible and fast segmentation techniques are desired.

Although there is little literature on automated segmentation of treated sites during RF ablation, segmentation techniques for US images have been reported for applications with echocardiographic (*e.g.*, Corsi et al. 2002; Angelini et al. 2005), breast (*e.g.*, Horsch et al. 2002; Chang et al. 2003a) and prostate data (*e.g.*, Shen et al. 2003; Gong et al. 2004). Because of characteristic US artefacts, such as speckle and shadowing, intensity inhomogeneities, low contrast and ill-defined boundaries, simple image feature-based thresholding or edge-detection methods are ineffective. Successful segmentation algorithms reported for US images are based on morphologic operations (Czerwinski et al. 1999; Gong et al. 2004), neural networks (Binder et al. 1999), wavelet analysis (Angelini et al. 2001) and Markov random fields (Haas et al. 2000; Xiao et al. 2002; Brusseau et al. 2004; Gong et al. 2004). These incorporate preprocessing for speckle reduction (*e.g.*, the "stick" method) (Czerwinski et al. 1999), anisotropic diffusion (Perona and Malik 1990) and intensity corrections (Xiao et al. 2002).

Active contour models (Kass et al. 1987) are used as the basis of many techniques in medical image segmentation (McInerney and Terzopoulos 1996). An initial contour is placed in an "energy field" defined by the image data, and the contour is then iteratively deformed to the desired shape and position by minimizing an energy function. The energy function is defined in terms of internal energy (*i.e.*, contour shape, continuity, smoothness) and external energy (*i.e.*, image features such as the intensity and the gradient of the intensity and possibly other user-defined external constraints). Contours may be represented explicitly (known as parametric active contours also known as "snakes") (Kass et al. 1987) or implicitly as level sets of a higher dimensional scalar function, taking into account the intrinsic geometry of the contour (known as a geometric active contour based on contour evolution methods) (Osher and Sethian 1988). Both parametric (*e.g.*, Sebbahi et al. 1997; Chang et al. 2003b) and geometric (*e.g.*, Pathak et al. 1997; Corsi et al. 2002) active contour models have been used in segmentation of CT, magnetic resonance imaging (MRI) and US images. Our work applies a parametric active contour model to US-based elastography.

A variant of active contours called gradient vector flow (GVF) snakes was introduced by Xu and Prince (1998) to improve performance of contour segmentation. The GVF active contour has a larger capture range (*i.e.*, it is less sensitive to contour initialization) and exhibits better convergence to boundary concavities than conven-

tional snakes. This technique has recently been used in US for segmenting breast tumors in B-mode images (Chang et al. 2003b) and for tracking cardiac wall excursions in echocardiography (Sanchez et al. 2000). Because of the expected superior performance of this methodology, the GVF snake was chosen for segmenting thermal lesions in elastograms in this study. Our previous work (Techavipoo et al. 2004) presented a semiautomated segmentation method based on simple morphologic operations. We did not find other papers reporting segmentation of elastographic images.

The purpose of this paper was to describe a fully automated method to segment stiff lesions from the background in 2-D and 3-D elastographic data sets for cross-sectional area and volumetric measurements. The proposed algorithm is based on a coarse-to-fine transformation (Gaussian pyramid) (Burt and Adelson 1983) for active contour initialization and a gradient vector flow active contour model for deformable contour optimization, with the help of prior knowledge of the geometry of general thermal coagulations.

MATERIALS AND METHODS

Elastogram production

RF ablation *in vitro* was performed on specimens of freshly excised canine liver tissue (refer to Varghese et al. 2003 for details). A total of 44 RF coagulations were created, scanned and measured to obtain the thermal coagulation area and volume. An Aloka SSD 2000 (Aloka, Tokyo, Japan) real-time US scanner with a 42-mm 5-MHz linear-ray transducer with a 70% band width was used. 3-D elastographic data were produced by acquiring RF echo data before and after 0.5% compressions from scan planes separated by 2-mm increments. In general, about 15 scan planes contained the thermal coagulation. Time-domain cross-correlation analysis of the echo signals from the pre- and postcompression data sets for each image plane was performed. A window length of 3 mm with a 75% overlap between data segments was used to compute tissue displacements. Axial strain was estimated using a least squares strain estimator (Kallel and Ophir 1997) with a kernel size of 2.25 mm. After US scans, the liver specimens were fixed in a formalin solution for at least 2 weeks and then sliced in 2-mm intervals. The tissue slices were placed on a transparent film and photographically scanned. These fixed gross-pathology images were used to obtain volume estimations of the thermal coagulation.

Automated segmentation

The gradient vector flow snake algorithm (Kass et al. 1987; Cootes et al. 1994) was used for automatic segmentation of thermal lesions. A snake is defined as an energy-minimizing spline, where the snake energy depends on the contour shape and location in the image. To construct the contour of a thermal lesion, we first placed a circular spline on the central image of a 3-D data set. Its energy was then minimized through spline deformation. Local minima of this energy correspond to desired image properties.

The contour is defined parametrically as $X(s) = [x(s),y(s)]$, where $s\epsilon$ [0,1] is the normalized arc length along the contour. The energy functional to be minimized is (Kass et al. 1987):

$$E_{\text{total}} = \int_0^1 \left[\alpha(s)\left|dX(s)/ds\right|^2 + \beta(s)\left|d^2X(s)/ds^2\right|^2\right]ds + \int_0^1 E_{\text{ext}}(X(s))ds, \quad (1)$$

which is a sum of the internal energy of the snake (first term) caused by bending, and the external energy (second term) based on image properties. $\alpha(s)$ and $\beta(s)$ govern the relative influence of terms that specify the "continuity" and "smoothness" of the snake, respectively. Minimizing E_{total} can be done by solving Euler's equation (Kass et al. 1987) because, in our application, we used $\alpha(s) = \alpha$ and $\beta(s) = \beta$ (constants):

$$\alpha X''(s) - \beta X''''(s) - \nabla E_{\text{edge}} = 0, \quad (2)$$

where the primes mean derivatives. The lesion boundary we are looking for is a closed, circular-like contour. Therefore, the external energy used for thermal coagulation segmentation was based only on the edge features in the image:

$$E_{\text{ext}} = E_{\text{edge}} = -\left|\nabla[G_\sigma(x,y)^* I(x,y)]\right|^2, \quad (3)$$

where $I(x,y)$ is the grey level of the elastogram image and $G_\sigma(x,y)$ is a blur function perpendicular to the contour's orientation at (x,y). Euler's equation can also be viewed as a force balance equation:

$$F_{\text{int}} + F_{ext} = 0 \quad (4)$$

The internal force, F_{int}, discourages stretching and bending while the external potential force, F_{ext}, pulls the snake toward the desired image edges of thermal lesions. In homogeneous regions of the image, F_{ext} is nearly zero. Therefore, no force drives the snake to the desired boundary. To overcome this, the gradient vector flow (GVF) snake method (Xu and Prince 1998) defines a new external force field, $V(x,y) = [u(x,y)v(x,y)]$, which is the vector field that minimizes the energy functional:

$$E = \int\int \mu(u_x^2 + u_y^2 + v_x^2 + v_y^2) + \left|\nabla E_{\text{edge}}\right|^2 \left|V + \nabla E_{\text{edge}}\right|^2 dxdy, \quad (5)$$

where μ is a regularization parameter controlling the

trade-off between the first term and the second term in the integrand and whose value depends on the noise in the image, and u_x, v_x, u_y, and v_y are partial derivatives with respect to x and y. In a homogeneous region, the first term dominates and provides a slowly varying field. In the region close to the object boundary, the second term dominates and is minimized by setting $V = -\nabla E_{\text{edge}}$. $V(x,y)$ cannot be written as a potential force like the traditional snake. It starts from the force equalization function and replaces the term ∇E_{edge} in eqn (2) with $V(x,y)$. Note that eqn (3) is used in eqn (5) to calculate $V(x,y)$.

$V(x,y)$ was calculated by treating u and v as a function of time and solving the diffusion equations iteratively as discussed in (Xu and Prince 1998). After computing $V(x,y)$, the snake $X(x,y)$ was solved by perturbation and iteration methods discussed in Kass et al. (1987).

Contour initialization is the first critical step for the snake algorithm. The initial contour generally has to be close to the desired contour to avoid being trapped in a local minimum of the energy function that does not correspond to the true object boundary. Interactive algorithms generally need image-specific initialization (Yezzi et al. 1997; Corsi et al. 2002; Horsch et al. 2002; Wolf et al. 2002; Fenster and Downey 2003; Lin et al. 2003) and/or allow interactive correction of results (Koning et al. 2002; Wolf et al. 2002). Some procedures start by placing initial points of the contour close to the desired feature, using operators (Corsi et al. 2002; Fenster and Downey 2003; Lin et al. 2003) or an initial seed (Yezzi et al. 1997; Horsch et al. 2002; Wolf et al. 2002). For images that contain two distinct regions, manual initialization may be substituted by an initial curve-detection scheme to make the segmentation fully automated. For example, a tumor boundary in a breast image may be detected by automatic thresholding followed by morphologic operations, and the boundary between blood and an arterial wall may be computed by separating regions with different statistical properties of the US image texture (Chang et al. 2003a, 2003b; Shen et al. 2003).

Although GVF snakes have a larger capture range than traditional snakes, initialization of the contour is still critical to successful segmentation. To relax the initialization constraint, we used a coarse-to-fine segmentation approach. The use of a single choice of resolution generally does not produce good segmentation. This is because, at a coarse level, a coagulation boundary is not accurately delineated because of smoothing that reduces shape detail. On the other hand, fine resolution representations contain many edges and very jagged and spurious boundaries. However, a multiresolution approach, in which boundaries are detected at a range of scales, tracing the boundary detected from coarse resolution down through the highest resolution yields accurate spatial localization.

A flowchart for the segmentation process is presented in Fig. 2a. To accomplish the multiresolution approach, a Gaussian pyramid (Burt and Adelson 1983) was constructed by hierarchically convolving the original image with a spatial Gaussian kernel, smoothing with Gaussians (low pass filters) and resampling at each level. The pixel value in a level was the weighted average of pixel values in the next lower level. Each level in the pyramid represents the image at 1.5 times lower resolution than the image in the level below it. Neighboring pixels in an upper-level image are more independent because subsampling reduces their correlation. The snake algorithm was applied level by level, starting with the lowest resolution image in the pyramid and interpolating the result of one level as the initial contour for the next higher resolution level. We took steps to ensure that the initial contour was inside the coagulation using the mechanism described below. If it is initialized, even partially, outside the coagulation area, it will be attracted as much by other edges of the image as by the coagulation boundary, and most of the spurious edges are outside the coagulation area, especially at the distal side of the coagulation because the signal-to-noise ratio is low in the elastogram because of US shadowing effect. The final contour for a given image plane was the output of the snake after applying the interpolated result to the highest resolution image of the pyramid.

To achieve fully automatic segmentation, as shown in Fig. 2a, template matching at a coarse level of the Gaussian pyramid was performed first to determine an initial contour for the snake. Template matching on the low-resolution image is fast and relatively immune to noise. Thermal coagulations are stiffer than surrounding tissue and show as dark regions on an elastogram with a light background. Because we had prior knowledge that the thermal coagulation is spherical or ellipsoidal in shape because of the RF ablation technique used and the tissue response to heating, circular disks of variable sizes ($r = 0.3$ cm to 1.5 cm), with an outer ring having an area the same as the central disk, were used as trial templates. The goals were to find the location and size of template that matched the elastogram image. The best matching position was defined where the normalized cross-correlation of the template and image was maximum. If a simple disk were used as the template, any homogeneous region in the elastogram image could yield high correlation with the template. However, the disk-annulus template avoids this complication.

We chose a circular template instead of an ellipsoidal template based on prior knowledge of lesion shapes, as stated above. Because the number of degrees of free-

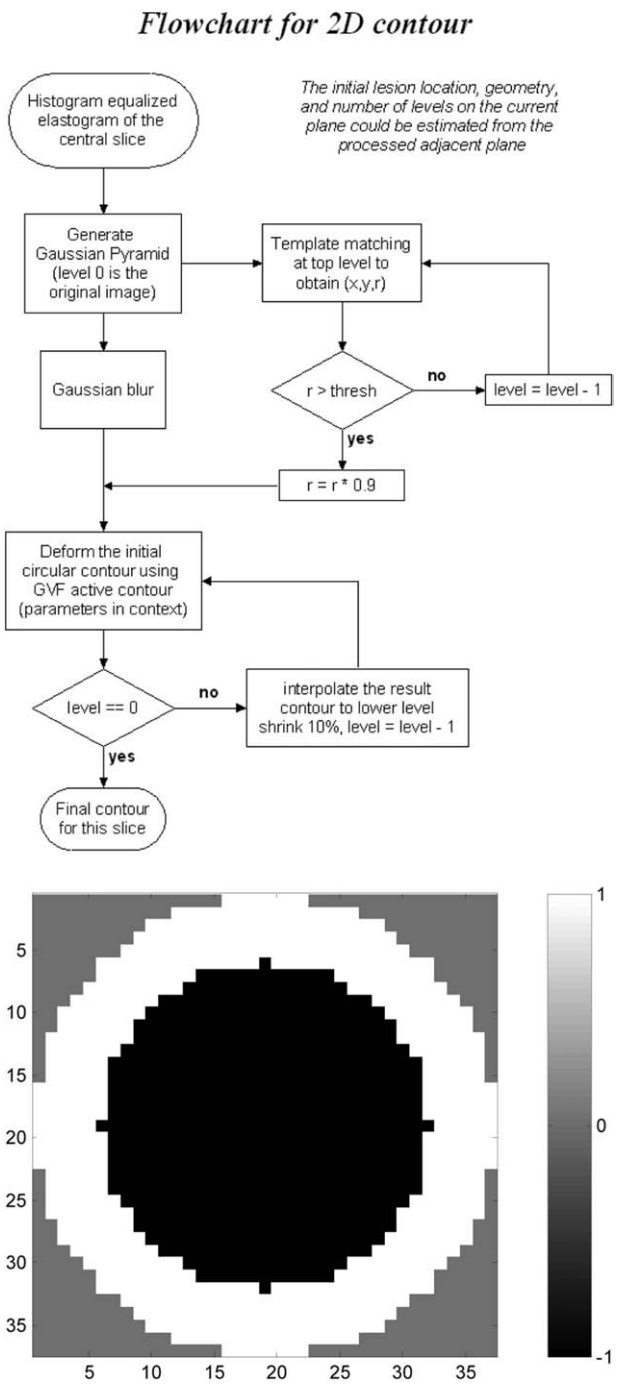

Fig. 2. (a) Flowchart for the segmentation process and (b) an example of the matching templates used. The area of the outer ring equals the area of the inner circular disk.

dom is less, computation time for template matching was saved without losing performance. A fast algorithm based on the fast Fourier transform was used to compute the cross-correlation. Figure 2b is an example of the matching templates used.

In the 3-D data sets in this study, there was a 2-mm elevational separation between elastograms. This was a compromise dictated by the need to acquire both pre- and postcompression data sets, the use of a manual translation system and the desire to do the experiment on a statistically significant number of thermal lesions. Thus, plane-to-plane image features were not sufficiently consistent in terms of the edges of the lesions to warrant the use of a full 3-D active surface. Furthermore, simple interpolation in the elevational direction may introduce artifacts.

Because 3-D data are essentially reconstructed from 2-D slices, the 2-D algorithm described above was applied repeatedly on the sequence of 2-D images, starting with the central plane of the 3-D data set and then moving to adjacent planes. The number of levels used in the Gaussian pyramid for the central slice was determined by an initial estimate of the lesion size in pixels from the template-matching result. The number depends on the resolution of the image and the size of the coagulations. We wanted the lesion radius to be represented by at least 10 pixels at the top level (lowest resolution) of the pyramid to ensure that edge information had sufficient detail to be detected by the active contour. For each plane after the central one, an initial lesion location, geometry and number of levels was estimated from the processed, adjacent plane. The Gaussian blurring kernel size σ used was 0.7 to 2 pixels, and was larger at higher resolution levels of the pyramid.

RESULTS

Figure 3 shows the performance of the active contour method at different resolution levels for three 2-D cases from our elastographic data. The rightmost images are the original elastograms (level 0 in the Gaussian pyramid containing the highest resolution). The leftmost images are level 3 images, and level 2 and level 1 images are in between. Higher level images are rescaled to the size of the original images for display only. On each image, the dashed line represents the initial contour and the solid line shows the computed contour. On the lowest resolution level, the snake was initialized by template matching, as mentioned in the previous section. Note that the initial contours here are circles. Instead of using the best matching circle for this initialization, we used a circle with a center the same as the center of the best matching circle, and a radius that was 90% of the radius of the best matching circle. This approach ensured that the initial contour would be inside the coagulation. The deformed snake computed for the lowest level was interpolated to the next level and shrunk 10% to serve as the initial guess for that level. This continued recursively until level 0 was reached. Notice, in Fig. 3, that the snake is gradually refined at the finer scales. Nevertheless, the

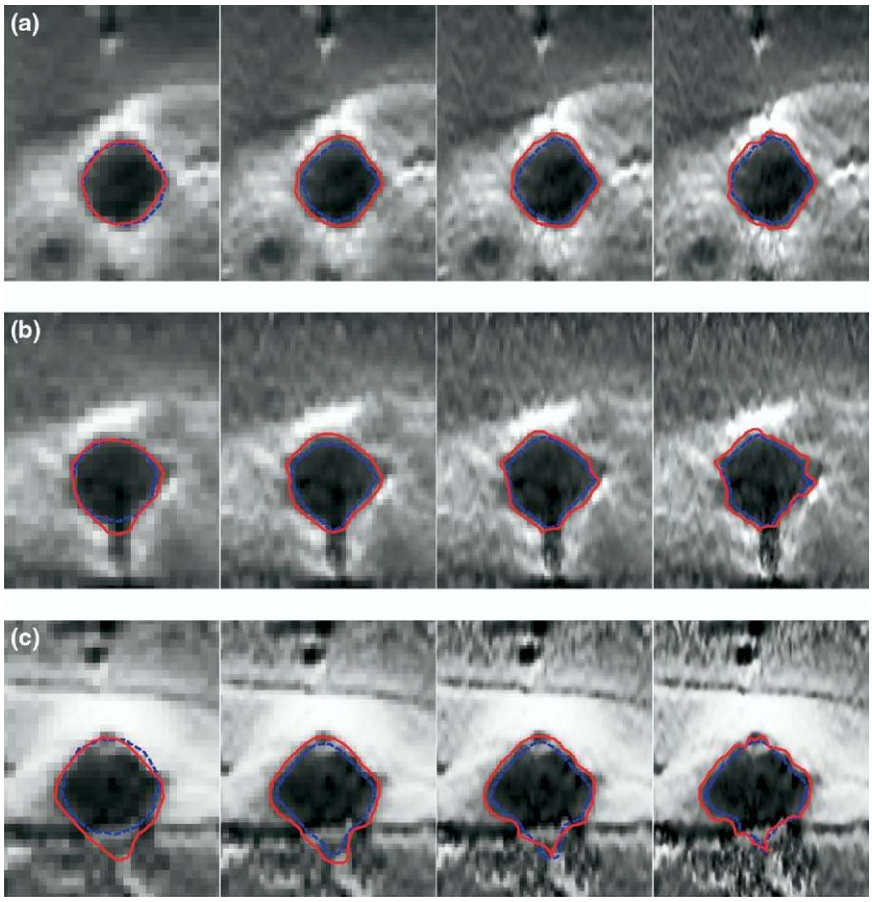

Fig. 3. Performance of the active contour method at different resolution levels for three 2-D cases (top panel (a), middle panel (b) and bottom panel (c)) from our elastographic data. (right) Original elastograms (level 0 in the Gaussian pyramid, or the highest resolution). (left) Level 3 images; (center) level 2 and level 1 images. Higher level images are rescaled to the size of the original images for display purposes. On each image, dashed line = the initial contour and the solid line = the computed contour

.

boundary shape for each level generally remained similar to that of other levels.

To give an example of the performance using different initial contours, eight data sets were randomly selected (two each from 70°, 80°, 90° and 100° ablation temperatures, respectively, yielding coagulations of different sizes). Thermal lesions in elastographic images for these data sets were segmented using different sized initial contours. We compared the results using 1.0*r, 0.9*r, 0.7*r and 0.5*r as the radius of the initial contour, where r is the template size that yields the maximum correlation with the image slices. The results of this comparison are listed in Table 1, where the extent of overlap of areas and volumes of thermal lesions segmented manually and segmented automatically are shown for different sized initial contours. The overlap was computed using overlap = (Manual ∩ Automated)/(Man-

Table 1. Extent of overlap of areas and volumes of thermal lesions on elasticity images segmented manually and segmented automatically, for different sized initial contours

Initial contour radius		0.9*r	1.0*r	0.7*r	0.5*r
Central slice area overlap (%)	Average	91.31	91.29	91.26	89.89
	SD	4.76	4.80	4.80	8.27
Volume overlap (%)	Average	85.41	85.28	84.36	82.50
	SD	5.52	5.44	6.93	9.34

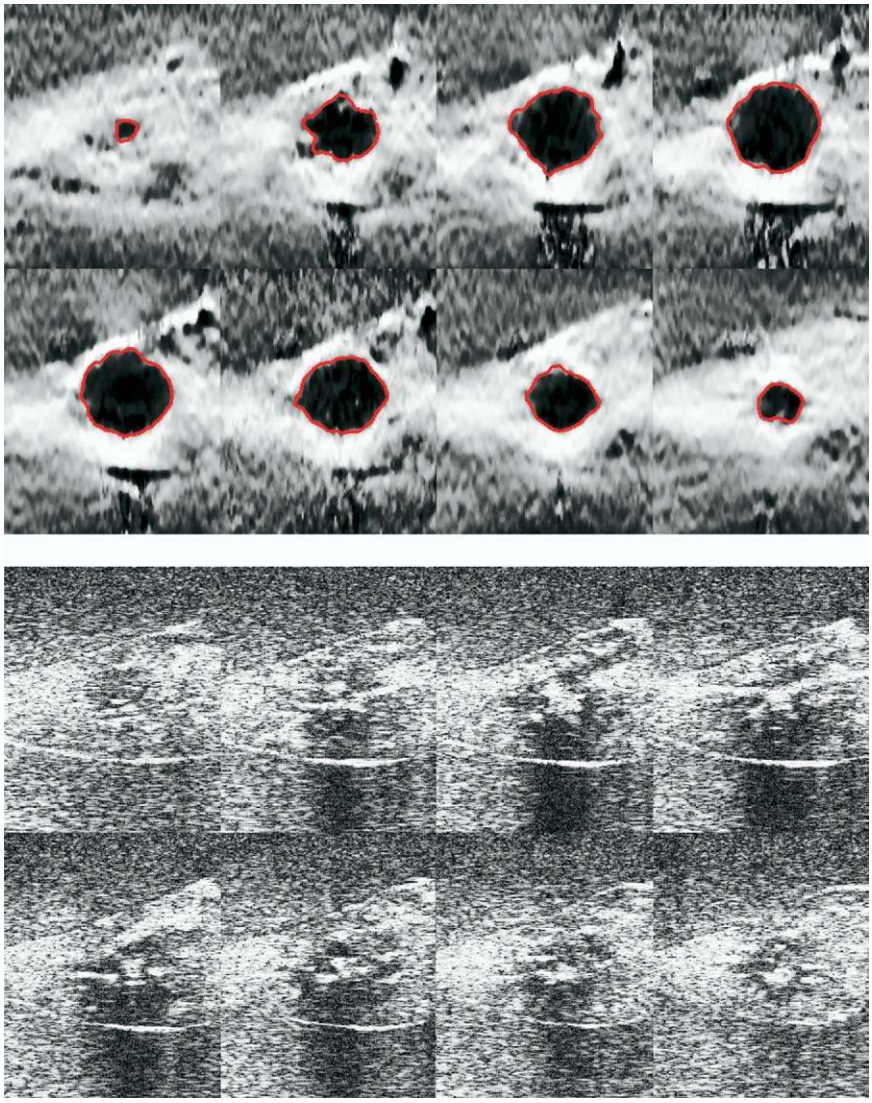

Fig. 4. A typical automated segmentation result for (a) a 3-D elastography data set and (b) its corresponding US B-mode images. Only the level 0 images are shown, and only every other slice from the 3-D volume is shown. Contours are the automated segmentation results.

ual ∪ Automated), where ∩ and ∪ represent intersection and union, respectively.

Table 1 shows that, when the radius of the initial contour was reduced to 0.5*r, the performance started getting worse. For initial contours greater than this size, but less than r, however, results appear to be similar regardless of the value. Although there is no difference between 1.0*r and 0.9*r in these eight random test cases, we used 0.9*r for all our data sets because of the reason discussed above.

With these steps, a reliable detection of the coagulation boundary was obtained. Fig. 3a is an ideal case for automated segmentation, which traced the stiffer region on the elastogram accurately. Figure 3b shows that, even if there are "difficult" regions to segment, caused, for example, by the area below the coagulation, the method is sufficiently robust to find a desired contour (*i.e.*, one that agrees with manual segmentation). Most of our experimental images are similar to those in Fig. 3a and b. However, a small percentage of images, as in Fig. 3c, yielded results obviously different from manual segmentation. In this example, the snake did not stop at the weak edge below the coagulation, but proceeded farther down; although, in finer resolution images, the result improved, as expected. Depending on the image quality, there may be zero, one or sometimes a few unsatisfactory slices in each 3-D set of elastograms. However, in every data set, there was sufficient information to estimate the lesion volume.

Figure 4a is a typical automated segmentation result

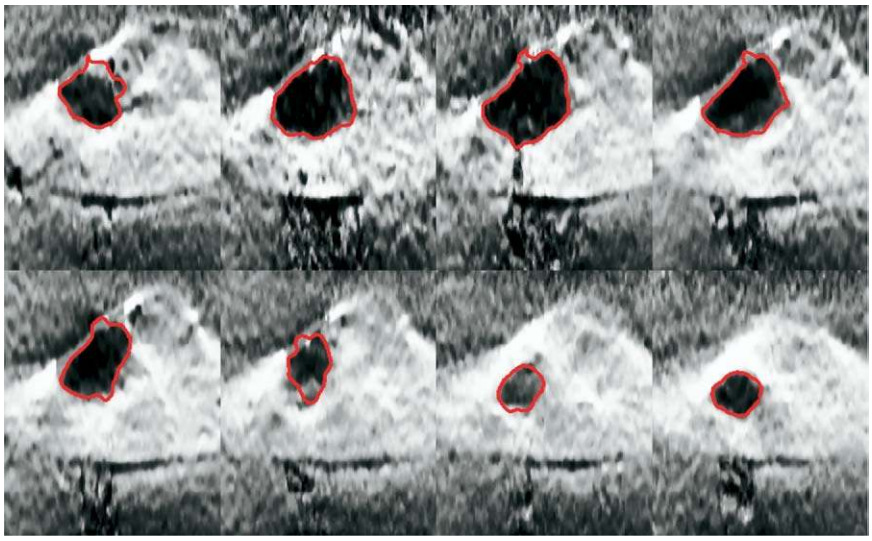

Fig. 5. Another example of an automated segmentation result for a 3-D elastography data set.

for a 3-D data set, and Fig. 4b presents the corresponding US B-mode images. Only the level 0 images are shown in Fig. 4a, and only every other slice from the 3-D volume is shown. Contours are segmentation results. This result shows how, after selecting the initial contour in the central slice, the algorithm successfully segmented the coagulation in each remaining slice. Figure 5 is another example, showing that the method gives desirable results for a more difficult case.

For further tests, parameters used for the algorithm were chosen by applying the algorithm on the training set (first eight thermal coagulations we acquired) and visually judging the desirability of final contours. This set of parameters was then used for the remaining 36 coagulations, for example, $\alpha = 0.6$ and $\beta = 0.3$ in eqn (2); $\mu = 0.1$ in eqn (5). However, we observed that, for most of our data, the final contours did not appear to be sensitive to the selection of parameter values, as long as they were within the neighborhood of values just mentioned.

Figure 6 is one of the 3-D surface reconstruction results for these thermal coagulations. The problem with 3-D surface reconstruction from a series of 2-D image slices is the lack of information between adjacent planes. An effective interpolation method or more data are desired for a better reconstruction.

Although automatic segmentation is the ultimate goal, manual tracing is still commonly used in clinics and is considered to be the most accurate and reproducible segmentation method for many problems. Based on 36 thermal coagulations, the average area overlap of the central slice elastograms was 89.5%. Using results for every image plane, the average volume overlap of the segmented coagulations was 84.3%. Figure 7 shows a scatterplot of coagulation volume measurements, comparing manually delineated volumes with automatically segmented volumes. They are highly correlated (correlation coefficient, r = 0.994), indicating that the automatically segmented results are very good if we assume manual depiction is the standard. Figure 8 displays scatterplots of coagulation volume measurements comparing manual or automated elastography volumes with fixed tissue pathology (manually depicted by a medical physicist). The correlation coefficient between manually delineated elastography volumes and pathology volumes is 0.972, and that between automated elastography volumes and pathology volumes is 0.967. Elastography tends to slightly underestimate the actual coagulation size found on gross pathology (Liu et al. 2004). However, the high correlation demonstrates that elastograms are valuable

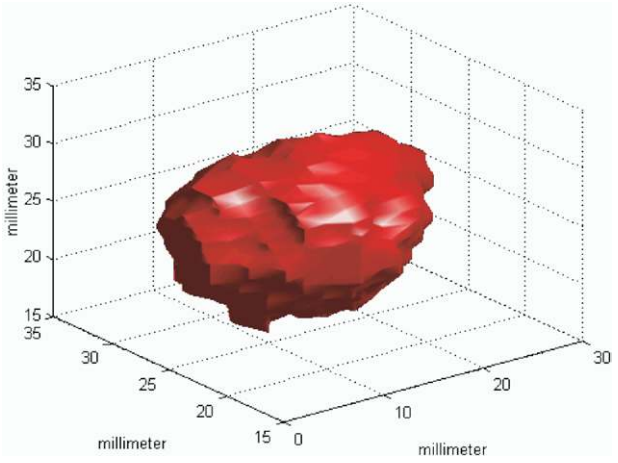

Fig. 6. An example of a 3-D reconstructed thermal coagulation surface.

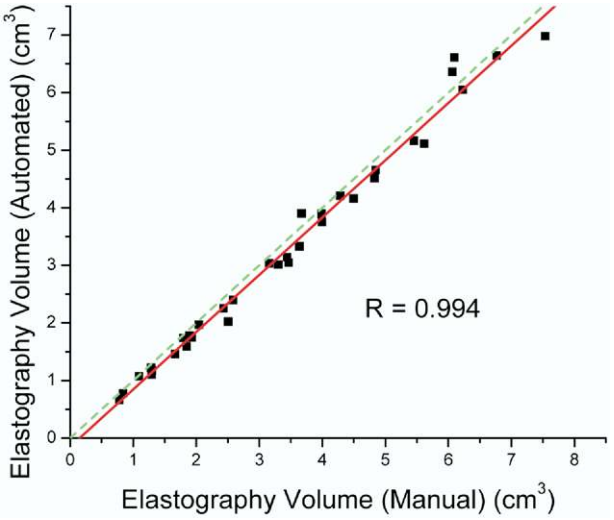

Fig. 7. Coagulation volumes obtained by manual depiction vs. volumes computed after automated segmentation. (—) From the least squares fit; (—-) the line of equal size.

for coagulation observation, and the results of Fig. 8 support the contention that the proposed segmentation algorithm can be used successfully for this application.

DISCUSSION

Our segmentation algorithm has the option of allowing users to examine the automated segmentation results and edit unsatisfactory parts interactively. This provides physicians with an automated segmentation tool to obtain diagnostically useful information quickly and accurately for most cases, and allowing full control over the results. Our goal is to segment not only rapidly but, also, accurately, instead of seeking the least possible user interaction, although we did not do any interactive correction when doing the automated-manual correlation analysis above.

The algorithm was implemented in Matlab version 7 (MathWorks Inc, Natick, MA, USA) and takes tens of seconds to process a 3-D image (about 15 slices) on a P4 2.8-GHz 1-GB RAM computer running Windows XP. The computationally intensive parts were written in C++ and incorporated into Matlab. In our data sets, the mean computation time for 3-D data set segmentation was 44.3 s, and the minimum and maximum execution times were 15.1 s and 110.5 s, respectively. Combined with the close correspondence between the manual and automated segmentation results, this demonstrates that the automated algorithm is able to provide quantitative thermal coagulation segmentations comparable to those obtained by manual delineation.

Although the results presented are for automated segmentation of *in vitro* ablation specimens, similar re-

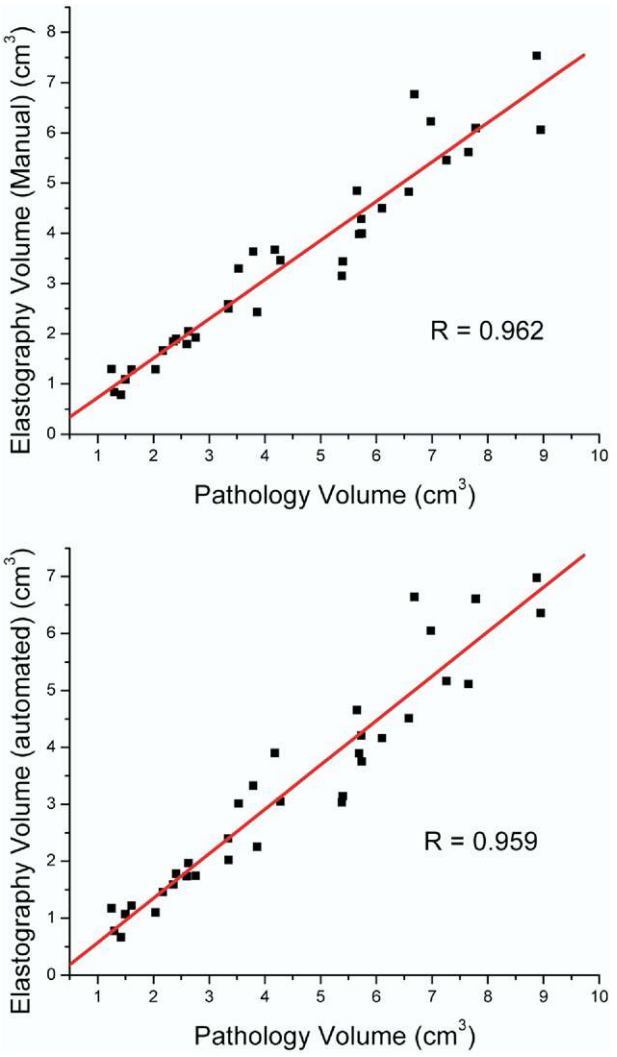

Fig. 8.
Coagulation volume measurements comparing (a) manual and (b) automated elastography volumes with volumes obtained from fixed tissue pathology.

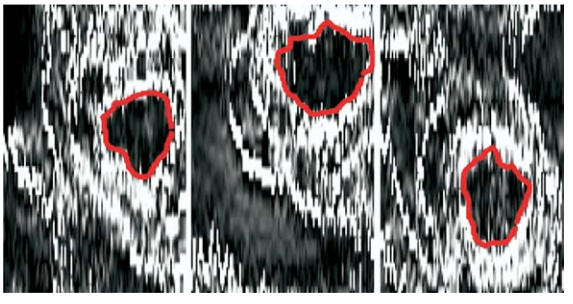

Fig. 9. Three examples of automated segmentation of thermal coagulations created in a pig liver *in vivo*.

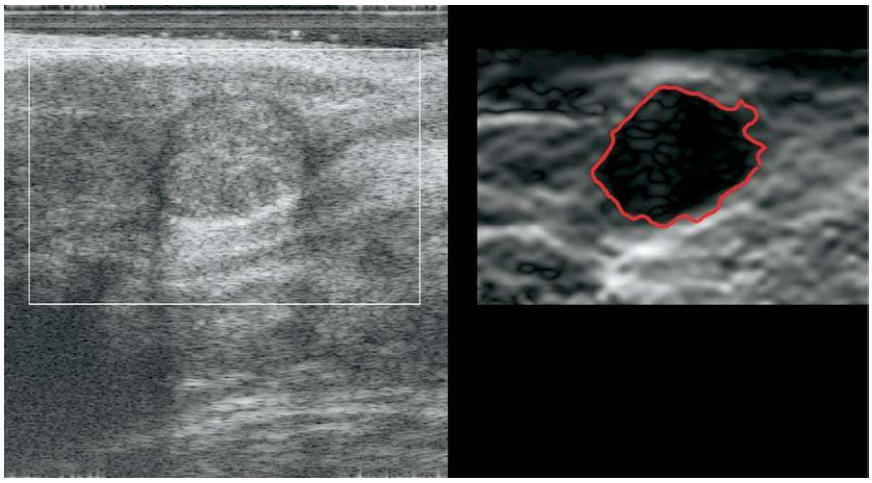

Fig. 10. An example of side-by-side, (left) synchronous real-time B-mode US and elasticity images in human breast *in vivo* with (right) the automated lesion segmentation result for the elasticity image.

sults are expected under *in vivo* conditions. To illustrate this, *in vivo* elastograms for thermal coagulations in pig liver were used to further test the algorithm (Varghese et al. 2002). Only 2-D images were acquired and tested at this time. However, the results are promising, as shown in Fig. 9. The elastogram image quality here is lower than the image quality for *in vitro* studies presented above, caused in part by use of the RF probe itself as the compressor, rather than use of an external plate compressor as was done in this study. Nevertheless, boundary depiction seems to agree with that that would be traced manually.

Another potentially significant application of this segmentation algorithm is for use in real-time breast elastography. A real-time elasticity imaging system has been developed (Zhu and Hall 2002; Hall et al. 2003) that provides side-by-side, synchronous B-mode US and elasticity images. The frame rate is high enough to control the boundary conditions of freehand deformation to consistently obtain high-quality elasticity images. Preliminary clinical trials with this system have demonstrated that elasticity imaging provides new information that is useful for diagnosing solid breast tumors (Regner et al. 2004). After a diagnosis of breast cancer has been made, the extent of disease must be assessed for treatment planning, prognosis and the evaluation of the efficacy of preoperative chemotherapy (Kepple et al. 2004). Several studies have demonstrated that B-mode ultrasonic imaging tends to underestimate the preoperative size of a tumor compared to pathology measurement (Pritt et al. 2004). More recent work (Hall et al. 2003; Regner et al. 2004) has shown that the size of a breast tumor is larger in elasticity images than shown in B-mode US images, and it is a reasonable hypothesis that the tumor size in elasticity images is a more accurate representation of that measured at pathology. Automated detection of tumor margin in breast elastography is desired for diagnostic uses. A preliminary segmentation result using the proposed algorithm is shown in Fig. 10. The computer-generated contour successfully delineated the breast lesion, suggesting that this may be a feasible approach.

The coarse-to-fine active contour method described here is effective for segmenting regions on images that have relatively regular, well-circumscribed single margins. Some clinical cases, however, might not exhibit this degree of regularity. Examples include speculated breast masses (Hall et al. 2003), thermal coagulations created using multiple RF probes (Lee et al. 2003) and coagulations formed near large blood vessels. Here, it may be worthwhile to investigate alternative segmentation methods, such as the watershed transformation and level sets. The watershed transformation (Beucher and Lantuejoul 1979) is a region-segmentation method using topographic and hydrology concepts. All points that drain into a common catchment basin are part of the watershed. However, morphologic or multiresolution methods may have to be applied to reduce oversegmentation, a characteristic of the algorithm. Level sets (Osher and Sethian 1988) refer to a contour evolution method that defines the problem in one higher dimension. It can handle features that the active contour method has difficulties with, including self-intersecting contours and changes in topology. Both the watershed transformation and levels sets have been applied for segmenting structures on B-mode images (Krivanek and Sonka 1998; Huang and Chen 2004; Angelini et al. 2005; Moon et al. 2005). Their role for elastographic image segmentation will be the topic of our future work.

SUMMARY

Automated segmentation of thermal coagulations viewed on 3-D elastograms can be achieved using active contours. A scheme involving a coarse-to-fine method for active contour initialization and a gradient vector flow active contour model for deformable contour optimization, with the help of prior knowledge of the geometry of general thermal coagulations, yields contour results that are comparable to those of manual delineation. This algorithm is suitable for evaluating its performance in *in vivo* applications of elastography.

Acknowledgements—This research was supported in part by the Whitaker Foundation (grant RG-02-0457) and the National Institutes of Health (grants R21EB002722, R21CA100989 and R01CA100373).

REFERENCES

Angelini ED, Homma S, Pearson G, Holmes JW, Laine AF. Segmentation of real-time three-dimensional ultrasound for quantification of ventricular function: A clinical study on right and left ventricles. Ultrasound Med Biol 2005;31:1143–1158.

Angelini ED, Laine AF, Takuma S, Holmes JW, Homma S. LV volume quantification via spatiotemporal analysis of real-time 3-D echocardiography. IEEE Trans Med Imaging 2001;20:457–469.

Antoch G, Kuehl H, Vogt FM, Debatin JF, Stattaus J. Value of CT volume imaging for optimal placement of radiofrequency ablation probes in liver lesions. J Vasc Interv Radiol 2002;13:1155–1161.

Beucher S, Lantuejoul C. Use of watersheds in contour detection. In: International Workshop on Image Processing, Real Time Edge and Motion Detection/Estimation, Rennes, France, 1979.

Binder T, Sussner M, Moertl D, et al. Artificial neural networks and spatial temporal contour linking for automated endocardial contour detection on echocardiograms: A novel approach to determine left ventricular contractile function. Ultrasound Med Biol 1999;25: 1069–1076.

Brusseau E, de Korte CL, Mastik F, Schaar J, van der Steen AF. Fully automatic luminal contour segmentation in intracoronary ultrasound imaging—A statistical approach. IEEE Trans Med Imaging 2004;23:554–566.

Burt P, Adelson EH. A multiresolution spline with application to image mosaics. ACM Trans Graphics 1983;2:217–236.

Cha CH, Lee FT Jr, Gurney JM, et al. CT versus sonography for monitoring radiofrequency ablation in a porcine liver. AJR Am J Roentgenol 2000;175:705–711.

Chang RF, Wu WJ, Moon WK, et al. Segmentation of breast tumor in three-dimensional ultrasound images using three-dimensional discrete active contour model. Ultrasound Med Biol 2003a;29:1571–1581.

Chang RF, Wu WJ, Tseng CC, Chen DR, Moon WK. 3-D snake for US in margin evaluation for malignant breast tumor excision using Mammotome. IEEE Trans Inf Technol Biomed 2003b;7:197–201.

Cootes T, Hill A, Taylor CJ, Haslam J. Use of active models for locating structure in medical images. Image Vision Comput 1994; 12:355–365.

Corsi C, Saracino G, Sarti A, Lamberti C. Left ventricular volume estimation for real-time three-dimensional echocardiography. IEEE Trans Med Imaging 2002;21:1202–1208.

Czerwinski RN, Jones DL, O'Brien WD Jr. Detection of lines and boundaries in speckle images—Application to medical ultrasound. IEEE Trans Med Imaging 1999;18:126–136.

De Sanctis JT, Goldberg SN, Mueller PR. Percutaneous treatment of hepatic neoplasms: A review of current techniques. Cardiovasc Intervent Radiol 1998;21:273–296.

Fenster A, Downey DB. Three-dimensional ultrasound imaging and its use in quantifying organ and pathology volumes. Anal Bioanal Chem 2003;377:982–989.

Fenster A, Downey DB, Cardinal HN. Three-dimensional ultrasound imaging. Phys Med Biol 2001;46:R67–R99.

Giorgio A, Tarantino L, de Stefano G, et al. Percutaneous sonographically guided saline-enhanced radiofrequency ablation of hepatocellular carcinoma. AJR Am J Roentgenol 2003;181:479–484.

Goldberg SN, Charboneau JW, Dodd GD III, et al. Image-guided tumor ablation: proposal for standardization of terms and reporting criteria. Radiology 2003;228:335–345.

Goldberg SN, Gazelle GS, Mueller PR. Thermal ablation therapy for focal malignancy: a unified approach to underlying principles, techniques, and diagnostic imaging guidance. AJR Am J Roentgenol 2000;174:323–331.

Gong L, Pathak SD, Haynor DR, Cho PS, Kim Y. Parametric shape modeling using deformable superellipses for prostate segmentation. IEEE Trans Med Imaging 2004;23:340–349.

Haas C, Ermert H, Holt S, et al. Segmentation of 3-D intravascular ultrasonic images based on a random field model. Ultrasound Med Biol 2000;26:297–306.

Hall TJ, Zhu Y, Spalding CS. *In vivo* real-time freehand palpation imaging. Ultrasound Med Biol 2003;29:427–435.

Hansler J, Neureiter D, Wasserburger M, et al. Percutaneous US-guided radiofrequency ablation with perfused needle applicators: Improved survival with the VX2 tumor model in rabbits. Radiology 2004;230:169–174.

Horsch K, Giger ML, Venta LA, Vyborny CJ. Computerized diagnosis of breast lesions on ultrasound. Med Phys 2002;29:157–164.

Huang YL, Chen DR. Watershed segmentation for breast tumor in 2-D sonography. Ultrasound Med Biol 2004;30:625–632.

Kallel F, Ophir J. A least-squares strain estimator for elastography. Ultrason Imaging 1997;19:195–208.

Kallel F, Ophir J, Magee K, Krouskop T. Elastographic imaging of low-contrast elastic modulus distributions in tissue. Ultrasound Med Biol 1998;24:409–425.

Kass M, Witkin A, Terzopoulos D. Snakes: Active contour models. Int J Comput Vision 1987;1:321–331.

Kepple J, Van Zee KJ, Dowlatshahi K, et al. Minimally invasive breast surgery. J Am Coll Surg 2004;199:961–975.

Koning G, Dijkstra J, von Birgelen C, et al. Advanced contour detection for three-dimensional intracoronary ultrasound: A validation—In vitro and in vivo. Int J Cardiovasc Imaging 2002;18:235–248.

Krivanek A, Sonka M. Ovarian ultrasound image analysis: Follicle segmentation. IEEE Trans Med Imaging 1998;17:935–944.

Lee FT Jr, Haemmerich D, Wright AS, et al. Multiple probe radiofrequency ablation: Pilot study in an animal model. J Vasc Interv Radiol 2003;14:1437–1442.

Lin N, Yu W, Duncan JS. Combinative multi-scale level set framework for echocardiographic image segmentation. Med Image Anal 2003; 7:529–537.

Liu W, Techavipoo U, Varghese T, et al. Elastographic versus x-ray CT imaging of radio frequency ablation coagulations: An in vitro study. Med Phys 2004;31:1322–1332.

McInerney T, Terzopoulos D. Deformable models in medical image analysis: A survey. Med Image Anal 1996;1:91–108.

Moon WK, Chang RF, Chen CJ, Chen DR, Chen WL. Solid breast masses: classification with computer-aided analysis of continuous US images obtained with probe compression. Radiology 2005;236: 458–464.

Ophir J, Cespedes I, Ponnekanti H, Yazdi Y, Li X. Elastography: A quantitative method for imaging the elasticity of biological tissues. Ultrason Imaging 1991;13:111–134.

Osher S, Sethian JA. Fronts propagating with curvature-dependent speed: Algorithms based on Hamilton–Jacobi formulations. J Comput Phys 1988;79:12–49.

Pathak SD, Chalana V, Kim Y. Interactive automatic fetal head measurements from ultrasound images using multimedia computer technology. Ultrasound Med Biol 1997;23:665–673.

Perona P, Malik J. Scale-space and edge detection using anisotropic diffusion. IEEE Trans Pattern Anal Machine Intell 1990;12:629–639.

Pritt B, Ashikaga T, Oppenheimer RG, Weaver DL. Influence of breast cancer histology on the relationship between ultrasound and pathology tumor size measurements. Mod Pathol 2004;17:905–910.

Regner DM, Hesley GK, Hangiandreou NJ, et al. Ultrasound strain imaging for the evaluation of breast lesions: Clinical experience of multiple observers. Radiology 2006 (in press).

Sanchez PJ, Zapata J, Ruiz R. An active contour model algorithm for tracking endocardiac boundaries in echocardiographic sequences. Crit Rev Biomed Eng 2000;28:487–492.

Sebbahi A, Herment A, de Cesare A, Mousseaux E. Multimodality cardiovascular image segmentation using a deformable contour model. Comput Med Imaging Graph 1997;21:79–89.

Shen D, Zhan Y, Davatzikos C. Segmentation of prostate boundaries from ultrasound images using statistical shape model. IEEE Trans Med Imaging 2003;22:539–551.

Techavipoo U, Varghese T, Zagzebski JA, Chen Q, Liu W. Semiautomated thermal lesion segmentation for three-dimensional elastographic imaging. Ultrasound Med Biol 2004;30:655–664.

Varghese T, Shi H. Elastographic imaging of thermal lesions in liver in-vivo using diaphragmatic stimuli. Ultrason Imaging 2004;26:18–28.

Varghese T, Ophir J, Konofagou E, Kallel F, Righetti R. Tradeoffs in elastographic imaging. Ultrason Imaging 2001;23:216–248.

Varghese T, Techavipoo U, Liu W, et al. Elastographic measurement of the area and volume of thermal lesions resulting from radiofrequency ablation: Pathologic correlation. AJR Am J Roentgenol 2003;181:701–707.

Varghese T, Zagzebski JA, Lee FT Jr. Elastographic imaging of thermal lesions in the liver in vivo following radiofrequency ablation: Preliminary results. Ultrasound Med Biol 2002;28:1467–1473.

Wolf I, Hastenteufel M, De Simone R, et al. ROPES: A semiautomated segmentation method for accelerated analysis of three-dimensional echocardiographic data. IEEE Trans Med Imaging 2002;21:1091–1104.

Xiao G, Brady M, Noble JA, Zhang Y. Segmentation of ultrasound B-mode images with intensity inhomogeneity correction. IEEE Trans Med Imaging 2002;21:48–57.

Xu C, Prince JL. Snake, shapes, and gradient vector flow. IEEE Trans Image Process 1998;7:359–369.

Yezzi A Jr, Kichenassamy S, Kumar A, Olver P, Tannenbaum A. A geometric snake model for segmentation of medical imagery. IEEE Trans Med Imaging 1997;16:199–209.

Zhu Y, Hall TJ. A modified block matching method for real-time freehand strain imaging. Ultrason Imaging 2002;24:161–176.